Heteroepitaxy route to substrate limited epitaxial Co_2TiSn thin films by sputter beam epitaxy

Ridwan Nahar,[1] Riley Nold,[1] Naomi Derksen,[1] Don Heiman,[2,3] Michelle E. Jamer,[4] Gaurab Rimal,[5] Asghar Kayani,[5] and Adam J. Hauser[1]

[1]*Department of Physics and Astronomy, The University of Alabama, Tuscaloosa, Alabama 35487, USA*
[2]*Physics Department, Northeastern University, Boston, Massachusetts 02115, USA*
[3]*Physics Department, United States Naval Academy, Annapolis, Maryland 21402, USA*
[4]*Western Michigan University, Kalamazoo, Michigan 49008, USA*
[5]*Plasma Science and Fusion Center, MIT, Cambridge, Massachusetts 02139, USA*

(Received 6 November 2024; accepted 22 January 2025; published 10 February 2025; corrected 1 April 2025)

We report a substrate-limited, high-quality thin film growth of Co_2TiSn, requiring the use of a substrate-limited TiN buffer layer as well as a Nb capping layer to achieve an x-ray diffraction rocking curve full width at half-maximum of 12 arcseconds. This value represents more than an order of magnitude improvement over previous results for TiN, and more than two orders of magnitude better than any previous Co_2TiSn thin film reported. Our surface analysis of the TiN film grown on a-plane sapphire reveals a distinctive step-edge-guided nucleation and epitaxial layer growth. Additionally, our first-principles calculations on Co_2TiSn in its $L2_1$ and XA phases examine the limitations of various exchange correlation functionals and the impact of Hubbard U correction on accurately representing the magnetic properties and density of states of Co_2TiSn. The observed lower-than-ideal magnetic moment in the disordered (XA) phase corresponds well with the experimentally observed reduced magnetization of the Co_2TiSn film, as no evidence of phase segregation or secondary phase is detected. This work serves as both a roadmap for making high-quality Heusler alloy thin films and a stepping stone for the evaluation of the intrinsic atomic ordering in this and other Heusler systems by providing a high-quality crystal with energetics during formation as close to the thermodynamic limit as possible.

DOI: 10.1103/PhysRevMaterials.9.024401

I. INTRODUCTION

Cobalt-based Heusler compounds have garnered considerable research interest in recent years due to their potential applications in spintronic devices [1] and shape memory technologies [2]. These compounds offer desirable properties such as high Curie temperatures [3,4], substantial magnetic moments [5,6], and high spin polarization [7,8], making them promising candidates for various technological advancements. In many cases, the fabrication of Heusler compounds in thin film form is essential to fully exploit their potential [2,9].

The choice of substrate material plays a critical role in thin film growth processes as substrates serve as templates that significantly influence the properties and performance of the resulting films [10,11]. Achieving high-quality thin films in complex epitaxial structures is widely known to require the selection of high-quality substrates with minimal epitaxial mismatches [12,13]. However, cost and availability of the substrate materials play an important role in this selection process and researchers often need to balance performance requirements and economic factors. Although oxide substrates are widely used due to their availability and specific properties, there are certain considerations and challenges associated with them in thin film deposition processes [14]. Differences in thermal expansion coefficients and lattice mismatch between oxide substrates and thin film materials can induce stress during cooling, resulting in the formation of defects, delamination, or other structural issues in the thin film. Moreover, oxygen atoms in oxide substrates may diffuse into the growing thin film, particularly at higher temperatures, altering its stoichiometry and resulting in nonuniform composition [15,16].

To address these challenges, researchers often employ buffer layers as a strategy to obtain desired properties of the thin film. In metal-on-oxide epitaxy, metallic buffer layers are important in preventing island growth and secondary phases. Numerous previous studies have explored various buffer layer systems [17–20], with TiN emerging as a highly promising candidate. TiN films have been found to exhibit good thermodynamic stability, exceptionally high melting points, good diffusion resistance, and good adhesion to most oxide materials [21–24].

This study focuses on Co_2TiSn, a half-metallic ferromagnet of considerable interest due to its half-metallic property [25,26] with Weyl points at the Fermi surface [26,27]. The difference in valence electron charges between Co and Ti atoms results in distinct local potentials at each site making it more effective in preventing atomic disorder between Co and Ti atoms compared to Co and Cr/Mn/Fe [28]. While extensively studied in bulk form [26,29–31], there is limited research on the high-quality growth of Co_2TiSn thin films. Meinert *et al.* reported epitaxial growth of Co_2TiSn films with a full width at half-maximum (FWHM) of 0.6° (2160 arcsec) on magnesium oxide (MgO) substrates at a growth temperature of 600 °C [32]. Shamardin *et al.* recently reported films with a full width at half-maximum (FWHM) of 0.2° (680 arcsec) on MgO substrate at a growth temperature of 700 °C, and detailed beautifully the relative roughness borne

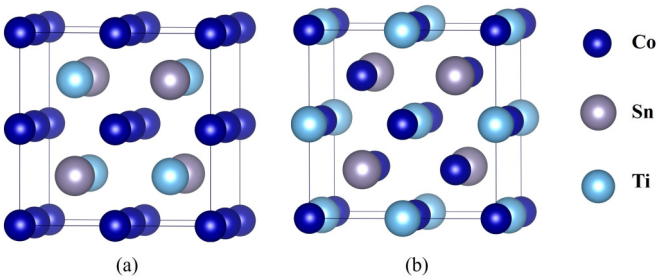

FIG. 1. (a) Schematic representation of ordered ($L2_1$) and (b) disordered (XA) structure of Co_2 TiSn.

of three-dimensional growth when growing the metallic alloy on an oxide substrate [33]. Suharyadi *et al*. utilized a Cr-buffer layer on MgO (001) substrates to grow $L2_1$-ordered Co_2TiSn films at growth temperatures between 200 and 600 °C [34]. Previous studies commonly employed MgO and Si substrates due to their lower mismatch with the alloy. However, achieving high-quality single-crystal films with smooth surfaces remains challenging [24,32,34,35]. In contrast, Al_2O_3, despite its higher anisotropic mismatch compared to MgO, holds promise for producing high-quality single-crystal thin films when coupled with a carefully selected buffer layer, such as TiN.

In this study we present the epitaxial growth of Co_2TiSn thin film on Al_2O_3 substrates using a TiN buffer layer. The film and buffer layers repeatably show substrate-limited rocking-curve (RC) FWHMs of roughly 12 arcseconds, and nearly atomically smooth surfaces without surface defects and in the case of TiN on a-plane sapphire, well-defined unit cell step edge growth. Although MgO has a suitable lattice parameter for TiN buffer layer growth, we were unable to produce consistent high-quality TiN thin films to date and will only report the comparative difficulty here.

Additionally, density functional theory (DFT) simulations were utilized to investigate the ground-state properties of the cubic ternary Co_2TiSn Heusler alloy, providing insights into its fundamental characteristics and behavior under different computational methods. The Co_2TiSn ternary Heusler compound, with a 2:1:1 stoichiometry, can crystallize in the regular ($Fm\bar{3}m$, space group 225) or inverse ($F\bar{4}3m$, space group 216) structure. Regular Heusler structures are spanned by four interpenetrating fcc sublattices at A(0, 0, 0), B(1/4, 1/4, 1/4), C(1/2, 1/2, 1/2), and D(3/4, 3/4, 3/4) sites. The sublattice sites A(0, 0, 0) and C(1/2, 1/2, 1/2) are occupied by Co atoms and the remaining sublattice sites B(1/4, 1/4, 1/4) and D(3/4, 3/4, 3/4) are occupied by Ti and Sn elements, respectively. For an inverse Heusler structure, one of the Co atoms interchanges position with the Ti atom (structure shown in Fig. 1). Previous studies have highlighted the sensitivity of Co-based Heusler alloys ground-state properties to the choice of DFT method [6,28,36,37]. It has been concluded that to obtain accurate ground-state properties of this alloy it is important to incorporate a full potential calculation method and/or include orbital-dependent electron electron correlation [38–40]. In our investigation, we demonstrated whether self-consistent calculations with a plane-wave pseudopotential method [41] can depict Co_2TiSn as either half-metallic or not using both a generalized gradient approximation (GGA) [42] and local density approximation (LDA) [43]. We also highlight the shortcomings of each of these methods.

A. Sample preparation and experimental methods

The deposition of Co_2TiSn films involved a three-step process with the following stack sequence: Substrate/TiN (10 nm)/Co_2TiSn (X nm)/Nb (2.0 nm). 10 nm TiN thin film buffer layers were deposited on both a-plane ($Al_2O_3(11\bar{2}0)$) and c-plane (Al_2O_3 (0001)) single crystal sapphire substrates using a custom-built off-axis Sputter Beam Epitaxy system by AJA International, Inc., with beam-shaping shutter control and growth rate tuning via quartz crystal microbalance (QCM). The system, equipped with six sputtering sources arranged in a confocal geometry, allows simultaneous sputtering from up to six sources with a base pressure typically at 5×10^{-9} Torr. During TiN deposition, a constant flow of 99.9999% pure 5 sccm Ar gas and 10 sccm of N_2 gas was supplied into the chamber. Three Ti targets were cosputtered simultaneously at a total deposition rate of about 0.75 Å/s for the TiN buffer layer growth.

Optimal growth conditions, including temperature, pressure, and deposition rates, were determined through analysis of x-ray diffraction (XRD) peak intensity, FWHM of RC measurements, and small-angle x-ray reflectometry (XRR) data. The best film quality, characterized by maximum (111) diffraction peak intensity and lowest FWHM, was achieved at a temperature of 1000 °C and a pressure of 5 mTorr ($Ar + N_2$). Prior to TiN deposition, all substrates underwent an *in situ* annealing step at 1000 °C for 15 min to remove volatile impurities. Subsequently, the substrates were cooled down to 500 °C in the presence of sputtering gas at 5 mTorr pressure ($Ar + N_2$).

For the growth of the Co_2TiSn thin film, two Ti targets, one Co target, and one Sn target were sputtered simultaneously at a total rate of about 1.8 Å/s. Prior to Co_2TiSn growth, N_2 flow was discontinued and all targets were presputtered for 5 min at 5 mTorr Ar pressure to remove target surface impurities and reach an equilibrium between the N_2 flow and any newly sputtered material on the chamber walls that may act as an effective absorption pump for the N_2. Following deposition, the substrates were cooled down *in situ* to room temperature, and a 2.0 nm Nb capping layer was deposited on top of the Co_2TiSn films to minimize oxidation before removing them from the chamber. The deposition rate was monitored using a quartz crystal microbalance (QCM), and film uniformity was improved by rotating the sample holder at 40 rpm.

XRD and XRR analyses were conducted using a Rigaku SmartLab x-ray diffractometer equipped with a Cu-$K_{\alpha 1}$ radiation source ($\lambda = 1.5406$ Å) to characterize crystal structure, epitaxial quality, and film thickness. Energy dispersive x-ray spectroscopy (EDS) on a Thermo Scientific Apreo Scanning Electron Microscope was employed to fine tune the stoichiometry of the Co_2TiSn films to a ratio of 2:1:1 (Co:Ti:Sn) with less than 5% uncertainty. Surface conditions were also evaluated using the same scanning electron microscope. The stoichiometry of the as-deposited Co_2TiSn thin films was further confirmed using Rutherford backscattering (RBS) analysis. RBS data were collected in a tandem van de Graaff

accelerator using 2.0 MeV He^+ at Western Michigan University. Magnetic properties were measured using a superconducting quantum interference device (SQUID) MPMS magnetometer from Quantum Design at Northeastern University.

B. Computational approach

To investigate the magnetic and electronic properties of Co_2TiSn compounds under various conditions, we performed density functional electronic structure calculations using the quantum espresso simulation package [44,45]. This investigation covered both the ordered ($L2_1$) and disordered (XA) configurations of the compound and we employed different levels of theory in order to comprehensively explore how the particular choice of DFT scheme and the introduction of disorder impact the computed magnetization. Our primary focus was on the electronic and magnetic properties of the Co_2TiSn alloy utilizing the plane-wave pseudopotential and projector-augmented-wave approaches [46] for both regular ($L2_1$) and inverse (XA) Heusler forms. Initially, we employed a Perdew, Burke, Ernzerhof (PBE) [47] version of the GGA exchange-correlation functional for the density of states (DOS) calculation. However, this approach resulted in occupied minority spin states at the Fermi level, compromising the anticipated half-metallicity of the system. While GGA is a widely adopted exchange-correlation functional with proven success in various materials [48], it tends to overestimate bond lengths and lattice constants and underestimate electron-electron on-site correlation [38,49]. Previous studies have shown that both the LDA and GGA schemes fall short in accurately describing the electronic structure of Co-based alloys [50]. On the other hand, a notable enhancement in accuracy has been observed with the utilization of a DFT + U method, which incorporates an orbital-dependent electron-electron correlation, an essential aspect that is absent in standard LDA and GGA schemes [51,52]. In our calculations, we employed the Perdew-Zunger (PZ) [53] version of LDA for parametrizing the exchange-correlation energy functional. We further employed an effective Coulomb-exchange interaction term ($U_{\text{eff}} = U - J$, where U and J are the Coulomb and exchange parameter) for both the GGA and LDA schemes to determine whether the inclusion of correlation resolves the discrepancy between the theoretical and measured magnetic moment.

The chosen U_{eff} values for the calculations are 1.92 eV for Co and 1.36 eV for Ti. These values are close to the values for the Coulomb interaction U_{dd} for d electrons in the elemental 3d transition metal (as reported in Ref. [54]) and previously demonstrated efficacy in obtaining correct magnetic moments of Co- and Ti-based alloys [6,55]. The convergence of the total energy to a minimum value of 10^{-9} Ry serves as the criterion for the convergence of the self-consistent calculations. For k-space integration, we utilized a $20 \times 20 \times 20$ Monkhorst-Pack k-point mesh, resulting in 256 k points in the irreducible part of the Brillouin zone.

The conjugate-gradient (CG) method [56,57] was used to optimize the lattice structure. All calculations were spin-polarized with ferromagnetic alignment of spins. The minimum energy unit cell lattice parameter, or equilibrium unit-cell volume, was determined through energy minimization with respect to volume by fitting the data to Murnaghan's equation of state [58]. The system was then allowed to relax with the cell shape and volume free to change until it reaches the ground state. A self-consistent calculation was performed on the relaxed structure to get the final cohesive energy of the system. To get the DOS and band structure, a non-self-consistent calculation was performed after the final self-consistent calculation.

II. RESULTS AND DISCUSSION

A. Structural characterization

Figures 2(a) and 2(b) show the $2\theta - \omega$ XRD pattern of ~34 nm uncapped TiN film grown on a and c-plane sapphire at 1000 °C. At this thickness, TiN films were found to be relaxed and the out-of-plane lattice constants obtained from the XRD peak positions were 4.248 ± 0.002 Å and 4.243 ± 0.001 Å, on a- and c-plane sapphire, respectively. The presence of pronounced Laue oscillations confirms that grown films are of high quality, homogeneous, with smooth and planar top and bottom interfaces. The FWHM obtained from the RC measurements was 198 asec and 135.7 asec for film grown on a-plane and on c-plane sapphire, respectively. While numerous studies have investigated TiN thin films on c-plane sapphire substrates [59–61], there is limited literature available regarding TiN films on a-plane sapphire. Smith *et al.* reported a high-quality TiN thin film on c-plane sapphire with a comparable FWHM to ours, measuring 0.0484° (174.2 asec) [59]. The achieved FWHM indicates a high-quality film. However, when TiN films are capped or, in our case, when Co_2TiSn films are *in situ* grown on them in ultrahigh vacuum, preventing the TiN layer from exposure to oxygen, the FWHM of TiN is reduced to as small as 12 arcsec. The quality of the film is also evident from the atomic force microscopy (AFM) images, Figs. 2(c) and 2(d). TiN film grown on a-plane sapphire clearly shows step-edge-guided nucleation and epitaxial layer growth, a unique characteristic not seen in other studies on TiN films grown on any plane of sapphire [60–63]. Steps are not visible for films grown on c-plane sapphire. However, the smooth surfaces create an ideal condition for subsequent material growth.

Figures 3(a) and 3(b) illustrate the out-of-plane $2\theta - \omega$ diffraction pattern of capped Co_2TiSn thin films of varying thicknesses, each deposited on a ~10 nm TiN buffer layer, which was deposited on $Al_2O_3(11\bar{2}0)$ and $Al_2O_3(0001)$ substrates. Figures 3(c) and 3(d) show small angle XRR data for TiN/ Co_2 TiSn/Nb thin film grown on Al_2O_3 substrates. The observed diffraction pattern reveals prominent TiN peaks corresponding to [111] orientation and Co_2 TiSn peaks corresponding to the [220] crystal orientation, with pronounced Laue oscillations indicative of a single-crystal structure.

To extract quantitative information from the XRR spectra, the Parratt formalism [64], as implemented in SmartLab Studio II, was employed. The fitting process facilitated the estimation of film thickness, roughness, and density of different layers of the films. Bragg's law was applied to manual calculation based on peak values to confirm out-of-plane lattice constants found via Studio II. The out-of-plane d-spacing of the approximately 10 nm TiN buffer layer on a-plane Al_2O_3

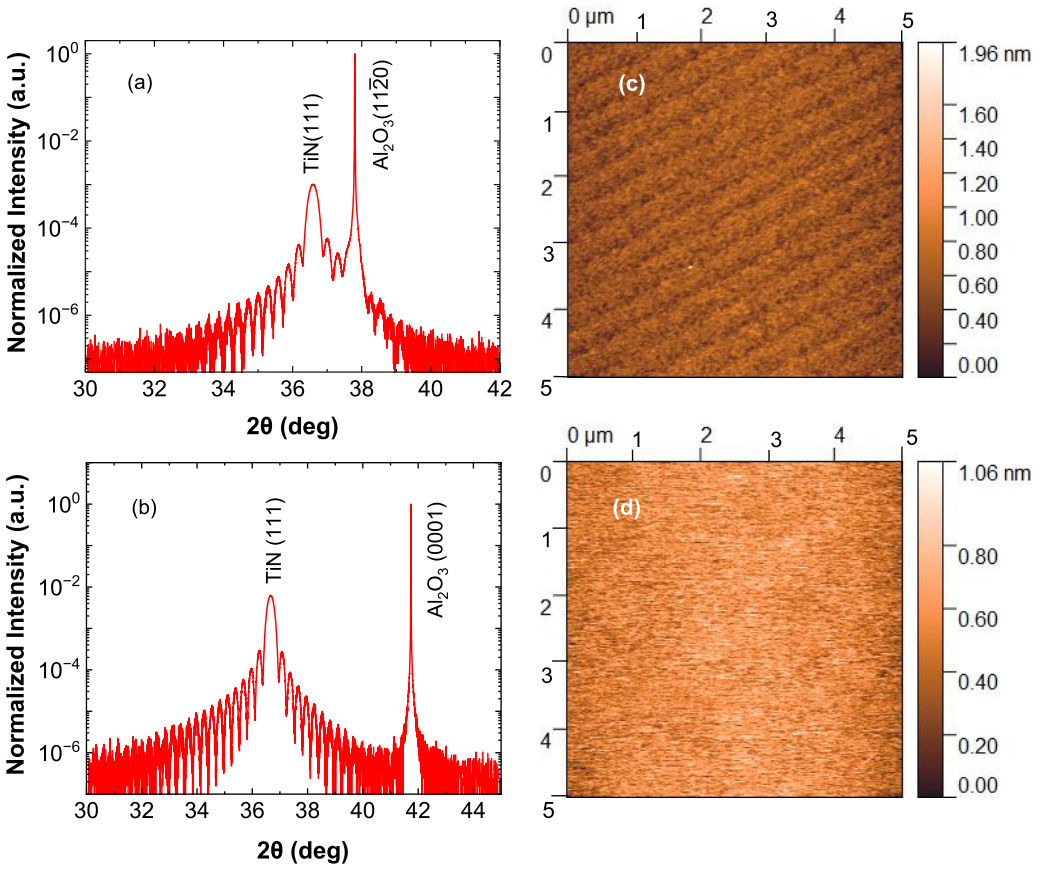

FIG. 2. 34 nm TiN thin films deposited on a- and c-plane sapphire substrates. [(a), (b)] XRD analysis of TiN films on sapphire substrates. [(c), (d)] Atomic force microscopy (AFM) images of the films on a- and c-plane sapphire, respectively.

substrate was found to be 2.448 Å, consistent with the bulk value. The TiN film grown on a c-plane sapphire substrate gives an out-of-plane <111 > d spacing of 2.44 Å, suggesting a small in-plane tensile strain.

Figures 3(a) and 3(b) display the out-of-plane XRD patterns for Co_2TiSn films of varying thicknesses. Pronounced Laue oscillations in these patterns indicate a smooth film interface. The out-of-plane (220) d-spacing of the 11.6 nm Co_2TiSn film grown on a-plane sapphire measures 2.15 Å, approximately 0.2% larger than the bulk value of 2.146 Å, suggesting a slight compressive epitaxial strain. Conversely, on c-plane sapphire, the out-of-plane (220) d spacing for the 11.5 nm Co_2TiSn film is 2.143 Å, almost comparable to the bulk value. However, on both types of films, the d spacing decreases to approximately the same value of 2.137 Å, and the lattice constant in the out-of-plane direction reaches 6.045 Å when the thickness exceeds 70 nm.

The FWHM values for RC measurements on all Co_2TiSn films are limited by the quality of the buffer and the presence of a capping layer. In Fig. 4(a), remarkable improvement of the Co_2TiSn FWHM via buffer layer is shown using 42.2 nm thick films grown (gray) directly on the sapphire substrate, with no buffer or cap, (red) with a 10 nm TiN buffer layer but no cap, and (blue) with both a 10 nm buffer layer and a 2.0 nm Nb capping layer. The FWHM of Co_2TiSn films grown on a TiN buffer is roughly a third of that grown directly on the oxide substrate. By placement of a Nb capping layer, the FWHM of the film is reduced from 200 asec to a ∼12 asec value limited only by the quality of the sapphire substrate.

Figure 4(b) illustrates the FWHM of the a-plane sapphire substrate, ∼10 nm TiN buffer, and ∼42.2 nm Co_2TiSn film grown on it with a ∼2.0 nm Nb cap for comparison. Both the TiN and Co_2TiSn FWHM values exhibit substrate-limited behavior, reaching remarkably small values of 11.88 and 12.24 arcsec, respectively. Our methods provide Co_2TiSn FWHMs far smaller than reported in prior existing literature [32,35,65–67]. The introduction of a metallic buffer layer likely changes the interfacial surface energy during growth, resulting in layer-by-layer growth instead of the island growth typical of metals and alloys grown directly on oxide substrates. The Nb capping layer serves to inhibit surface oxidation of the Co_2TiSn film, contributing to the marked FWHM improvement. We show below in Fig. 5 evolution in the film morphology, with changes in growth mode being a likely driving force for the improved morphology, uniformity, and crystallinity. The diffusion resistance quality of TiN may help prevent oxygen from the substrate from diffusing into the buffer layer, and the excellent thermodynamic stability of TiN limits interfacial mixing with the film at growth temperature.

Scanning electron microscopy (SEM) results presented in Figs. 5(a) and 5(b) reveal the surface condition of ∼40 nm Co_2TiSn film grown on Al_2O_3 $(11\bar{2}0)$ substrate with no buffer layer and with the 10 nm TiN buffer layer, respectively. The films were moved from the growth system directly to the vacuum of the microscope to minimize effects from

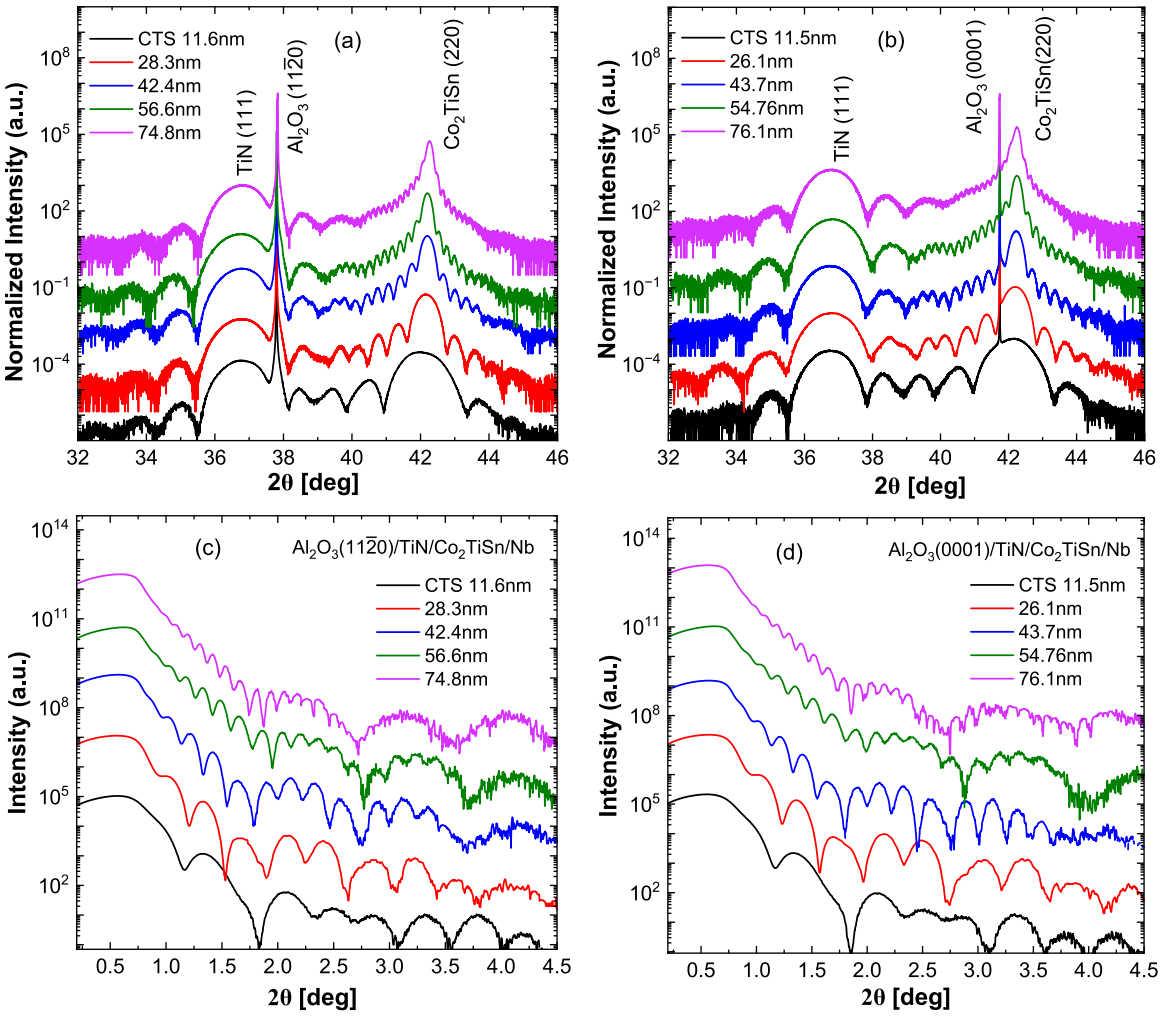

FIG. 3. $2\theta - \omega$ XRD scans of epitaxial TiN/Co_2TiSn thin films (vertically offset for clarity) on (a) Al_2O_3 $(11\bar{2}0)$ and (b) Al_2O_3 (0001) single-crystal substrates. $2\theta - \omega$ XRR scans of TiN/, Co_2TiSn films on (c) $Al_2O_3(11\bar{2}0)$ and (d) Al_2O_3 (0001) substrates demonstrate pronounced Kiessig oscillations with actual Co_2 TiSn film thickness reported.

surface oxidation. However, oxidation alone could not explain the striking difference observed: In the absence of a buffer layer, the Co_2TiSn film clearly exhibits a random three-dimensional (3D) island growth pattern with an average island size of 500 nm [(Fig. 5(a)]. This growth behavior resembles the Volmer-Weber type, characteristic of heteroepitaxial growth [68]. In our thickness range, the islands do not easily connect together as thickness increases and prefer to continue

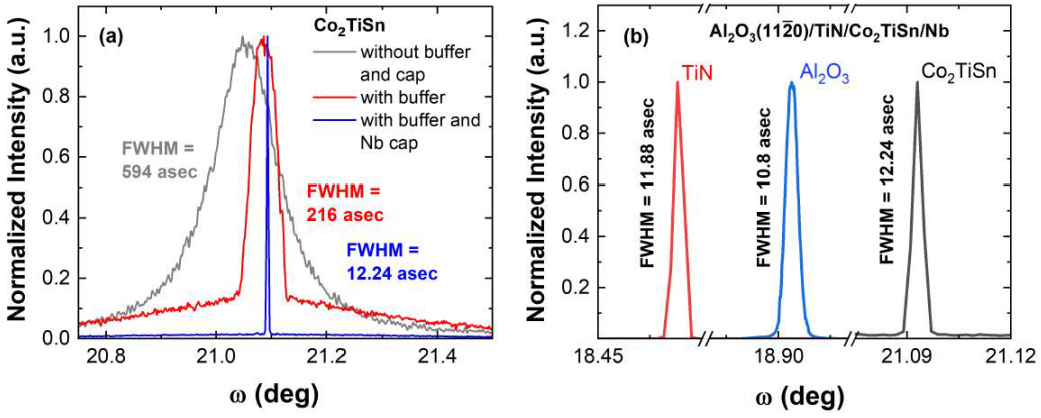

FIG. 4. (a) RC for (220) Bragg peak of ∼40 nm thick Co_2TiSn film on Al_2O_3 substrate grown with and without buffer and capping layer. (b) FWHM of the a-plane sapphire (Al_2O_3) substrate, ∼10 nm TiN buffer, and ∼42.2 nm Co_2TiSn film grown on it with an ∼2.0 nm Nb cap.

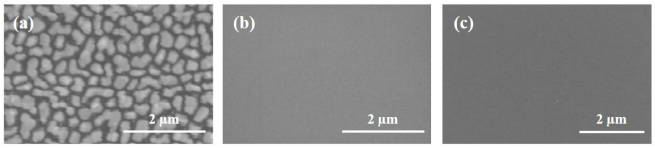

FIG. 5. Scanning electron microscopy (SEM) images of ∼40 nm Co_2 TiSn film with stacking sequence (a) $Al_2O_3(11\bar{2}0)/Co_2$ TiSn. (b) $Al_2O_3(11\bar{2}0)$/TiN/Co_2 TiSn; (c) $Al_2O_3(11\bar{2}0)$/TiN/Co_2TiSn /Nb.

to accumulate material on each isolated mesa, resulting in a tall cobblestone pattern when observed, a common result when epitaxial metal or alloy growth is attempted on an oxide substrate. EDS measurements find relatively uniform island compositions, suggesting that long-range mobility or phase segregation are not concerns here. On the other hand, when grown on a TiN buffer layer, Co_2TiSn films show a smooth 2D surface with an absence of defects and minimal roughness [Fig. 5(b)]. We note that adding the Nb capping layer to the film made no change to the surface morphology [Fig. 5(c)].

EDS measurements conducted on the same film without a buffer layer indicates nearly stoichiometric composition with a ratio of 1.95:1.0:1.03 if normalizing the Ti content to 1, or 1.96:1.0:1.04 if normalizing the sum composition to 4 as expected in an idealized Heusler alloy. Similar chemical composition assessments on a number of islands or positions within the films reveal consistent stoichiometry. SEM and EDS measurements conducted on all deposited films in the thickness series show only slight variation (±2%) within the margin of error of the EDS system, suggesting that the consecutively grown films share a similar composition.

However, for the films with buffer layers, distinguishing between the Ti contributions from the buffer layer and the Co_2TiSn film in films is challenging, and overall systematic errors from EDS are always possible and hard to quantify for any thin film. As such, we employed RBS (Rutherford backscattering spectrometry) analysis to confirm the composition of the Co_2TiSn thin film grown with a TiN buffer and Nb capping layer. RBS data (open circles) and simulated fits (red solid line) of Co_2TiSn films are shown in Fig. 6 and show that the films are nearly stoichiometric, with values of 48 at.% Co, 26 at.% Ti, and 26 at.% Sn, with approximate experimental uncertainties of ±1% for each element. It can be reasonably concluded that Co_2TiSn films are nearly stoichiometric with a probable-but-slight Co deficiency. From the analysis, thicknesses of the TiN buffer and Nb capping layers were found to be ∼8 nm and ∼1.5 nm, respectively. These values assume the high density of the ideal crystal structure with no defects, and are likely underestimations.

B. Magnetic properties

Magnetic hysteresis measurements were conducted at a temperature of 10 K on 74.8 nm and 76.1 nm Co_2TiSn films grown on a-plane and c-plane sapphire substrates, respectively, with Nb capping layers and TiN buffer layers. Saturation magnetizations of 1.51 ± 0.02 and 1.52 ± 0.02 μ_B per formula unit were found for films on a-plane and c-plane sapphire, respectively [Figs. 7(a) and 7(b)]. The coercivity of

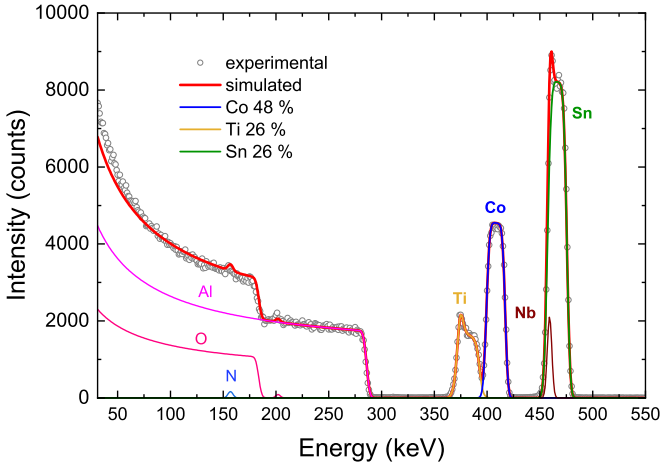

FIG. 6. RBS spectrum of Co_2TiSn thin film deposited on Al_2O_3 $(11\bar{2}0)$ substrate showing nearly stoichiometric Co_2 TiSn films, $Co_{1.93}$ $Ti_{1.02}$ $Sn_{1.04}$ within 1% accuracy.

the a-plane and c-plane-grown films were 50 ± 5 and 80 ± 2 Oe, respectively, consistent with previous reports in both bulk [29] and thin films [33]. The magnetization as a function of temperature (normalized to the value found at $T = 10$ K) upon heating under a magnetic field of 0.1 T is shown in Fig. 7(c). The data shows a Curie temperature (T_c) above room temperature for films grown on both substrate orientations. To refine our estimate of T_c, an Arrot plot analysis was conducted for the 76.1 nm Co_2TiSn film grown on Al_2O_3 (0001) (still with a TiN buffer and Nb cap layer). In-plane magnetic hysteresis curves were recorded from 0–0.6 T across a temperature range of 300–345 K in 5 K intervals [Fig. 8(a)]. Figure 8(b) depicts an Arrot plot (M^2 v.s. H/M) for the same data seen in Fig. 8(a). A least-squares regression line was determined for the linear region of the Arrot data for each fixed temperature. The zero-field ($H = 0$ T) value of the regression is taken as the squared spontaneous magnetization (M_{sp}^2) for each temperature, respectively. The temperature-dependent M_{sp}^2 data are reported in Fig. 8(c). Error bars on the M_{sp}^2 data were found to be smaller than the corresponding data symbols and are therefore not shown. A separate least-squares regression is calculated for the linear region of Fig. 8(c), providing an estimate of $T_c = 321.4 \pm 2.0$ K.

The low-temperature saturation magnetization values and Curie temperature are lower than previous reports of Co_2TiSn: In bulk samples, a Curie temperature of approximately 355 ± 5 K was reported by Barth *et al.* for a $Co_2Ti_{0.94}Sn_{0.83}$ sample as measured by energy-dispersive x-ray spectroscopy [66]. A saturation moment of 1.97 μ_B per formula unit is referenced but data is not shown. Naghibolashrafi *et al.* [29] reported a saturation moment of 2.11 μ_B/f.u. and a Curie temperature of 364 K for a carefully confirmed stoichiometric Co_2TiSn sample. Their work also showed that the magnetic moment and Curie temperature for Co-deficient $Co_{1.75}$TiSn film reduce to 1.68 μ_B/f.u. and 360 K, respectively, and subsequent reduction of Co content further reduces these values. The slight Co deficiency we suspect in this film cannot account for the change in T_c alone, as Naghibolashrafi *et al.* [29] found only

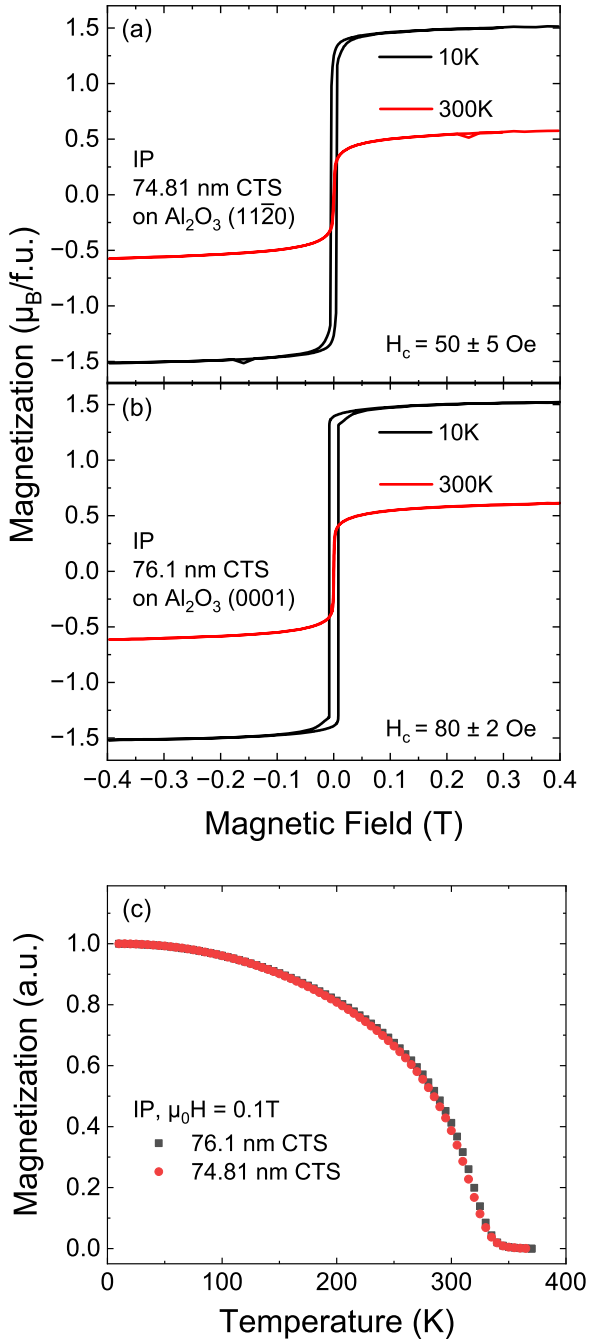

FIG. 7. [(a), (b)] In-plane (IP) magnetic hysteresis loops, *M(H)*, for Co_2TiSn films of 74.81 nm and 76.1 nm thickness on Al_2O_3 (11$\bar{2}$0) and Al_2O_3 (0001) substrates, respectively, with TiN buffer and Nb cap, measured at 10 K and 300 K. The coercive field at 10 K (H_C) is also reported. (c) Normalized temperature-dependent magnetic moment of the same films grown on Al_2O_3 (11$\bar{2}$0) (red dots) and Al_2O_3 (0001) (black dots) substrates at a constant field of 0.1 T. The lowest-temperature moment has been normalized to one.

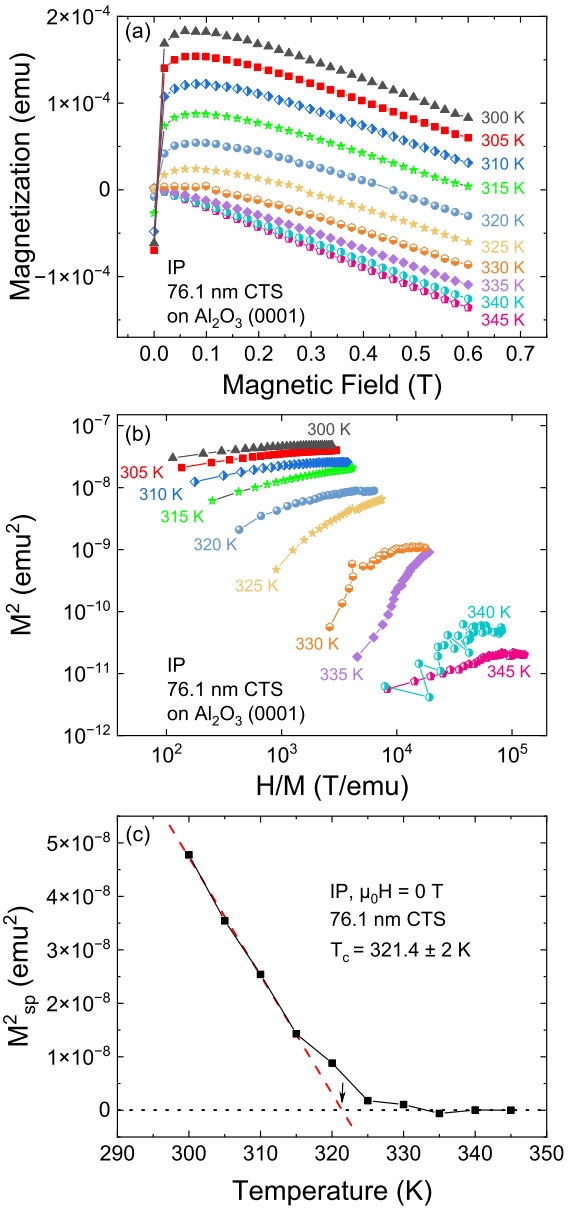

FIG. 8. [(a), (b)] In-plane (IP) *M(H)* curves and Arrot plot for 76.1 nm thick Co_2TiSn film grown on an Al_2O_3 (0001) substrate, with TiN buffer and Nb cap, measured from $T = 300$ K to $T = 345$ K in 5 K steps. (c) Squared spontaneous magnetization (M^2_{sp}) vs temperature for the same film. Error bars were much smaller than the data symbols and are not depicted. A least-squares regression line for the linear region is given (red dashed line). The intersection of the regression line with the $M^2_{sp} = 0$ axis (black dashed line) gives a $T_c = 321.4 \pm 2$ K estimate. The intersection point is noted with a black arrow.

a slight change in T_c when intentionally creating a much more severe Co deficiency in bulk.

Thin films grown on MgO substrates by Meinert *et al.* yielded a saturation magnetization of $1.6\,\mu_B$ per formula unit [32]. This result is in reasonable agreement with our work as, despite the difference in substrate/buffer layer choices, all films compared are nearly relaxed with only slight compressive strain. However, Meinert finds an elevated Curie temperature of 375 K, surprisingly higher than reported bulk values that typically exceed thin films when not or only lightly strained, but also measured through the temperature sweep at a lower field than the bulk works described above. We note a difference in shape between the magnetization vs temperature curves, though attribution of defects, disorder, morphological

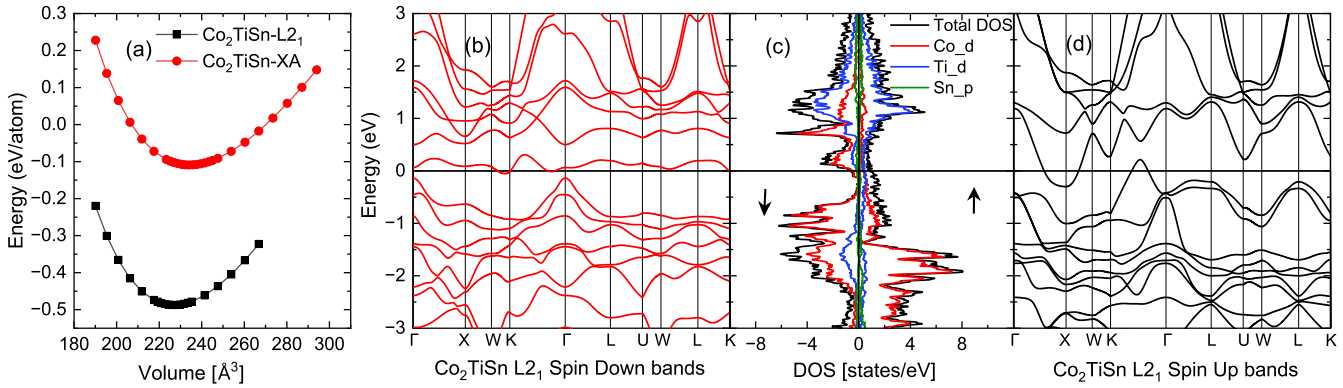

FIG. 9. (a) Energy-volume diagram for Co_2 TiSn in the $L2_1$ and XA phases. The solid line represents the fitting using the Birch-Murnaghan equation of state. (b) and (d) depict the spin-up and spin-down band structures of the $L2_1$ ordered Co_2 TiSn. (c) shows the corresponding DOS for these spin directions, with arrows indicating the spin direction and horizontal line representing the Fermi level.

differences or magnetic frustration via comparison is inappropriate given the different applied fields used in each study and lack of direct structural observation.

C. Electronic structure

The energy-volume relationship, band structure, and DOS of ordered and disordered Co_2TiSn were investigated using the PBE version of the GGA method, as illustrated in Fig. 9. Table I summarizes the computational details. Notably, a significant formation energy difference between the $L2_1$ and XA phases suggests a lower tendency for Co-Ti site-swap disorder in the system. While the GGA method accurately predicted a magnetic moment (M_{tot}) of $2\mu_B$ per formula unit for the $L2_1$ state, consistent with the Slater-Pauling rule [69] [$M_{\text{tot}} = Z_t - 24$; Z_t, total valence electron count, which is 26 with the configurations $3d^74s^2$ (Co), $3d^24s^2$ (Ti) and $5s^25p^2$ (Sn)], it failed in predicting the correct spin-down DOS near the Fermi level. Thus, further refinements such as using advanced exchange correlation functionals or a full potential treatment are necessary to address the observed discrepancies and fully characterize the electronic structure of Co_2TiSn.

In the original symmetrized structure presented in the introduction section, the two Co atoms occupying the X sites were expected to have identical moments. However, upon relaxation and adjustment of atomic positions, the symmetry between X1 and X2 sites is disrupted, leading to variations in the magnetic moments of these otherwise equivalent sites. This deviation from the symmetry resulting from the atomic relaxation procedure can be interpreted as a consequence of the resulting Jahn-Teller distortion [70,71]. Details about the calculation process, relaxed atomic positions, DOS, and pDOS (projected-DOS) data files are listed elsewhere [72].

The total density of states near the Fermi level is primarily influenced by the Co(d) and Ti(d) electrons. The dominant contribution to the total DOS originates from these Co(d) and Ti(d) electrons, with the pDOS of the Ti (Co) atom predominantly lying above (below) the Fermi level. A small indirect gap in the spin-down band just below the calculated Fermi level was observed in the $L2_1$ phase. However, such band-gap properties and integer moment of the ordered phase were disrupted in the presence of Co-Ti site-swapping disorder, as listed for the XA phase in Table I. Both GGA and LDA parametrizations produced discrepancies in the lattice constant with respect to previous experimental studies and severely underestimated the known high spin polarization of ordered Co_2TiSn.

The LDA method revealed certain distinct features of the Co_2TiSn band structure that could not be obtained by the GGA method. For instance, a flat band feature along the Γ-X symmetry direction can be seen in the spin-down band [Fig. 10 (blue rectangles)]. Additionally, clear band crossings between the conduction and valence bands are visible along the Γ-X and Γ-K directions in the spin-up bands [Fig. 10 (blue squares)]. Both of these features have been previously reported for the Co_2TiSn alloy band structure [27]. Typically, when there is only a flat band within a certain energy range, the DOS will exhibit a sharp peak at that specific energy. The slight deviation observed between the sharp peak in the DOS of Co_2TiSn and the flat band suggests the presence of other crossing bands at different symmetry points. Incorporating the +U correction on top of GGA and LDA parametrizations of the exchange-correlation functional proved instrumental in accurately reproducing the experimental magnetic moment and revealing a clear half-metallic gap around the Fermi level, thus confirming the half-metallic character of the material as

TABLE I. Summary of the computational details: calculated lattice constant, formation energy, spin polarization, total magnetic moment, site specific magnetic moments, and band gap for ordered ($L2_1$) and disordered (XA) phases of the Co_2TiSn alloy.

Phase	a (Å)	ΔE_{form} (eV/atom)	Spin Pol. %	M_{tot} (μ_B/f.u)	M_{Co1} (μ_B)	M_{Co2} (μ_B)	M_{Ti} (μ_B)	M_{Sn} (μ_B)	Gap width (eV)
$L2_1$	6.099	–0.174306	30	2.0	1.0118	1.0482	–0.059	0.0067	0.084 (Indirect)
XA	6.16	0.056612	76	1.62	0.4137	1.5251	–0.245	0.0164	-

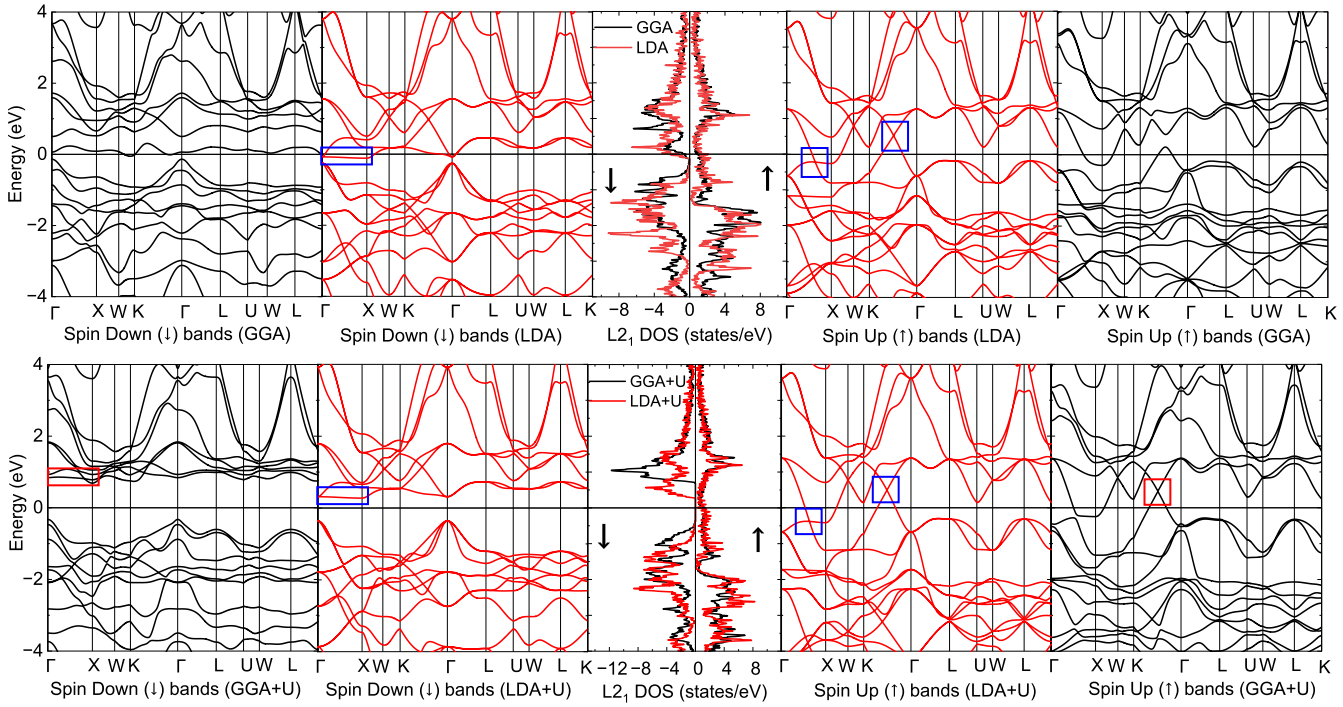

FIG. 10. Electronic structure of $L2_1$-ordered Co_2TiSn Heusler alloy in the absence of spin-orbit coupling. Shown are the band structure and DOS calculated without (top) and with (bottom) effective Hubbard U correction. Majority states are displayed on the right, minority states on the left, with arrows indicating the spin direction.

depicted in Fig. 10 and listed in Table II. The flat band feature of the spin-down bands and the band crossing in the spin-up bands in the Γ-K direction also appeared (red rectangle and square in Fig. 10) after applying the Hubbard correction to the GGA exchange correlation.

III. CONCLUSIONS

We have successfully grown phase-pure epitaxial thin films of Co_2TiSn using a TiN buffer layer on Al_2O_3 substrates, which is not the typical choice for Co_2TiSn thin film growth due to a larger epitaxial mismatch. The films were nearly stoichiometric with a slight Co deficit. The observed magnetic moments of 1.51 and 1.52 $\mu_B/f.u.$ (for films grown on a-plane and c-plane sapphire, respectively, and a Nb capping layer) and the T_c of 321.4 ± 2 K was significantly smaller than the reported bulk value. Previous results reported in the literature for thin films do not share enough structural information to make a definitive comparative analysis between works, but with no evidence of phase segregation or secondary phases, it is reasonable to expect large contributions from antisite disorder, which is known to have an outsized effect on magnetic moment in complex ordered materials, with even 10–15 % disorder resulting in a 25–40 % drop in magnetic moment, depending on the system [73–75]. Epitaxial strain and the Co deficit are both small and likely to play only secondary effects.

We conducted DFT calculations on Co_2TiSn in its $L2_1$ and XA Heusler phases. Our results revealed that using the GGA and LDA methods, without considering complete exchange correlation, severely underestimates the magnetic moment and yields incorrect DOS around the Fermi level. The effective Hubbard correction, represented by U_{eff}, incorporates the orbital dependence of Coulomb and exchange interactions, which are absent in LDA and GGA. Applying GGA + U and LDA + U methods resulted in a quantitative improvement in energy gaps around the Fermi level and ground-state properties, such as magnetic moments. It is worth noting that we calculate a reduced magnetization for Co_2TiSn in the XA phase, and although it may be tempting to make a claim of a different phase ordering, we must remember that the bulk result for this material is clear. As such, the most reasonable guess of the cause of the reduced magnetization remains

TABLE II. Summary of the computational details: calculated lattice constant, formation energy, spin polarization, magnetic moment(s), and band gap of ordered ($L2_1$) Co_2TiSn alloy using GGA, LDA, and Hubbard corrections.

Method	a (Å)	Cohesive Energy (Ry)	M_{tot} (μ_B/f.u)	M_{Co1} (μ_B)	M_{Co2} (μ_B)	M_{Ti} (μ_B)	M_{Sn} (μ_B)	Spin Pol. %	Gap width (Indirect, eV)
GGA	6.099	–1379.2738	2.0	1.0118	1.0482	–0.059	0.0067	30	0.084
GGA+U	6.115	–1378.9931	2.0	1.1226	1.1403	–0.2501	0.0009	100	1.015
LDA	5.949	–1355.4727	1.76	0.8663	0.8663	0.0234	0.0091	27.61	0.142
LDA+U	5.951	–1355.19187	2.0	1.0355	1.0355	–0.0121	0.0042	100	0.635

antisite disorder. Some disorder is likely a thermodynamic inevitability when formation energy differences (∼0.2 eV/atom) between phases are comparable to the combined thermal and incident material energies present during thin film formation.

ACKNOWLEDGMENTS

R. Nahar, R. Nold, and A.J.H. gratefully acknowledge financial support from the National Science Foundation (NSF CAREER DMR-2047251). A.J.H. and N.D. acknowledge support from the National Science Foundation under Grant No. 2328830, supported in part by funds from federal agency and industry partners as specified in the Future of Semiconductors (FuSe) program. Work at Northeastern University was partially supported by the National Science Foundation Grant No. DMR-1905662 and the Air Force Office of Scientific Research Award No. FA9550-20-1-0247. A.J.H. thanks K. Q. Twon for useful conversations and diversions.

DATA AVAILABILITY

The data that support the findings of this paper are not publicly available upon publication because it is not technically feasible and/or the cost of preparing, depositing, and hosting the data would be prohibitive within the terms of this research project. The data are available from the authors upon reasonable request.

[1] S. Wolf, D. Awschalom, R. Buhrman, J. Daughton, V. S. von Molnár, M. Roukes, A. Y. Chtchelkanova, and D. Treger, Spintronics: A spin-based electronics vision for the future, Science **294**, 1488 (2001).

[2] B. Winzek, S. Schmitz, H. Rumpf, T. Sterzl, R. Hassdorf, S. Thienhaus, J. Feydt, M. Moske, and E. Quandt, Recent developments in shape memory thin film technology, Mater. Sci. Eng., A **378**, 40 (2004).

[3] G. H. Fecher, H. C. Kandpal, S. Wurmehl, C. Felser, and G. Schönhense, Slater-pauling rule and Curie temperature of Co_2-based Heusler compounds, J. Appl. Phys. **99**, 08J106 (2006).

[4] M. Salaheldeen, A. Garcia-Gomez, P. Corte-Leon, M. Ipatov, V. Zhukova, J. Gonzalez, and A. Zhukov, Anomalous magnetic behavior in half-metallic Heusler Co_2FeSi alloy glass-coated microwires with high Curie temperature, J. Alloys Compd. **923**, 166379 (2022).

[5] J. Kübler, A. R. William, and C. B. Sommers, Formation and coupling of magnetic moments in Heusler alloys, Phys. Rev. B **28**, 1745 (1983).

[6] H. C. Kandpal, G. H. Fecher, and C. Felser, Calculated electronic and magnetic properties of the half-metallic, transition metal based Heusler compounds, J. Phys. D **40**, 1507 (2007).

[7] J.-C. Tung and G.-Y. Guo, High spin polarization of the anomalous hall current in co-based Heusler compounds, New J. Phys. **15**, 033014 (2013).

[8] K. Inomata, N. Ikeda, N. Tezuka, R. Goto, S. Sugimoto, M. Wojcik, and E. Jedryka, Highly spin-polarized materials and devices for spintronics, Sci. Technol. Adv. Mater. **9**, 014101 (2008).

[9] J. Venables, *Introduction to Surface and Thin Film Processes* (Cambridge University Press, Cambridge, 2000).

[10] N. Kaiser, Review of the fundamentals of thin-film growth, Appl. Opt. **41**, 3053 (2002).

[11] H. Liu, Growth kinetics of thin film epitaxy, *21st Century Surface Science—A Handbook* (IntechOpen, 2020).

[12] J. M. Phillips, Substrate selection for high-temperature superconducting thin films, J. Appl. Phys. **79**, 1829 (1996).

[13] J. M. Phillips, Substrate selection for thin-film growth, MRS Bull. **20**, 35 (1995).

[14] J. Schroeder, A. S. Ingason, J. Rosén, and J. Birch, Beware of poor-quality MgO substrates: A study of MgO substrate quality and its effect on thin film quality, J. Cryst. Growth **420**, 22 (2015).

[15] P. Panjan, A. Drnovšek, P. Gselman, M. Čekada, and M. Panjan, Review of growth defects in thin films prepared by PVD techniques, Coatings **10**, 447 (2020).

[16] C. W. Schneider, M. Döbeli, C. Richter, and T. Lippert, Oxygen diffusion in oxide thin films grown on $SrTiO_3$, Phys. Rev. Mater. **3**, 123401 (2019).

[17] W. Wu, K. Wong, and C. Choy, Epitaxial growth of $SrTiO_3$ films with different orientations on TiN buffered Si(001) by pulsed laser deposition, Thin Solid Films **360**, 103 (2000).

[18] J. Zhu, B. Lin, X. Sun, R. Yao, C. Shi, and Z. Fu, Heteroepitaxy of ZnO film on Si (111) substrate using a 3C–SiC buffer layer, Thin Solid Films **478**, 218 (2005).

[19] C. Jin, R. Narayan, A. Tiwari, H. Zhou, A. Kvit, and J. Narayan, Epitaxial growth of zinc oxide thin films on silicon, Mater. Sci. Eng., B **117**, 348 (2005).

[20] T.-U. Kim, B. R. Kim, W.-J. Lee, J. H. Moon, B.-T. Lee, and J. H. Kim, Integration of artificial $SrTiO_3$/$BaTiO_3$ superlattices on Si substrates using a TiN buffer layer by pulsed laser deposition method, J. Cryst. Growth **289**, 540 (2006).

[21] J. Narayan, P. Tiwari, X. Chen, J. Singh, R. Chowdhury, and T. Zheleva, Epitaxial growth of tin films on (100) silicon substrates by laser physical vapor deposition, Appl. Phys. Lett. **61**, 1290 (1992).

[22] R. Vispute, J. Narayan, K. Dovidenko, K. Jagannadham, N. Parikh, A. Suvkhanov, and J. Budai, Heteroepitaxial structures of $SrTiO_3$/TiN on Si(100) by in situ pulsed laser deposition, J. Appl. Phys. **80**, 6720 (1996).

[23] J. Narayan and B. Larson, Domain epitaxy: A unified paradigm for thin film growth, J. Appl. Phys. **93**, 278 (2003).

[24] P. Gupta, K. Sokhey, S. Rai, R. Choudhary, D. Phase, and G. Lodha, Pulsed laser ablated off-stoichiometric thin films of the Heusler alloy Co_2TiSn on Si (100) substrate, Thin Solid Films **517**, 3650 (2009).

[25] I. Galanakis, P. Dederichs, and N. Papanikolaou, Slater-pauling behavior and origin of the half-metallicity of the full-Heusler alloys, Phys. Rev. B **66**, 174429 (2002).

[26] A. Rahman, M. ur Rehman, D. Zhang, M. Zhang, X. Wang, R. Dai, Z. Wang, X. Tao, L. Zhang, and Z. Zhang, Critical behavior in the half-metallic Heusler alloy Co_2TiSn, Phys. Rev. B **100**, 214419 (2019).

[27] G. Chang, S.-Y. Xu, H. Zheng, B. Singh, C.-H. Hsu, G. Bian, N. Alidoust, I. Belopolski, D. S. Sanchez, S. Zhang *et al.*, Room-temperature magnetic topological Weyl fermion and nodal line semimetal states in half-metallic Heusler Co_2TiX (X = Si, Ge, or Sn), Sci. Rep. **6**, 38839 (2016).

[28] Y. Miura, M. Shirai, and K. Nagao, *Ab initio* study on stability of half-metallic Co-based full-Heusler alloys, J. Appl. Phys. **99**, 08J112 (2006).

[29] N. Naghibolashrafi, K. Shambhu, V. I. Hegde, J. Ma, A. Gupta, P. LeClair, W. Butler, C. Wolverton, and A. W. Ghosh, Synthesis and characterization of Co-Ti-Sn alloys: $Co_{1.5}TiSn$ as half-metal based on the $Fe_{1.5}TiSb$ layered Heusler prototype, J. Alloys Compd. **924**, 166501 (2022).

[30] I. Shigeta, Y. Fujimoto, R. Ooka, Y. Nishisako, M. Tsujikawa, R. Y. Umetsu, A. Nomura, K. Yubuta, Y. Miura, T. Kanomata *et al.*, Pressure effect on the magnetic properties of the half-metallic Heusler alloy Co_2TiSn, Phys. Rev. B **97**, 104414 (2018).

[31] M. Raïâ, R. Masrour, M. Hamedoun, J. Kharbach, A. Rezzouk, A. Hourmatallah, N. Benzakour, and K. Bouslykhane, Half-metalicity, mechanical, optical, thermodynamic, and thermoelectric properties of full Heusler alloys Co_2TiZ (Z = Si; Ge; Sn), Opt. Quantum Electron. **55**, 512 (2023).

[32] M. Meinert, J. Schmalhorst, H. Wulfmeier, G. Reiss, E. Arenholz, T. Graf, and C. Felser, Electronic structure of fully epitaxial Co_2TiSn thin films, Phys. Rev. B **83**, 064412 (2011).

[33] A. Shamardin, S. Cichoň, M. Rameš, E. de Prado, L. Volfová, T. Kmječ, L. Fekete, J. Kopeček, P. Kos, L. Nowak, J. Heicl, J. Zázvorka, J. Hamrle, M. Veis, O. Heczko, and J. Lančok, Growth and properties of full Heusler Co_2TiSn epitaxial thin films, J. Alloys Compd. **1002**, 175296 (2024).

[34] E. Suharyadi, T. Hori, K. Mibu, M. Seto, S. Kitao, T. Mitsui, and Y. Yoda, Nuclear resonant time spectra for ^{119}Sn in Co_2TiSn Heusler alloy films, J. Magn. Magn. Mater. **322**, 158 (2010).

[35] J. Hu, B. Ernst, S. Tu, M. Kuveždić, A. Hamzić, E. Tafra, M. Basletić, Y. Zhang, A. Markou, C. Felser *et al.*, Anomalous Hall and Nernst effects in Co_2 TiSn and Co_2 $Ti_{0.6}V_{0.4}$ Sn Heusler thin films, Phys. Rev. Appl. **10**, 044037 (2018).

[36] P. Tavadze, R. Boucher, G. Avendaño-Franco, K. X. Kocan, S. Singh, V. Dovale-Farelo, W. Ibarra-Hernández, M. B. Johnson, D. S. Mebane, and A. H. Romero, Exploring DFT + U parameter space with a Bayesian calibration assisted by Markov chain Monte Carlo sampling, arXiv:2109.07617.

[37] B. Himmetoglu, A. Floris, S. De Gironcoli, and M. Cococcioni, Hubbard-corrected DFT energy functionals: The LDA+U description of correlated systems, Int. J. Quantum Chem. **114**, 14 (2014).

[38] S. Wurmehl, G. H. Fecher, H. C. Kandpal, V. Ksenofontov, C. Felser, H.-J. Lin, and J. Morais, Geometric, electronic, and magnetic structure of Co_2 FeSi: Curie temperature and magnetic moment measurements and calculations, Phys. Rev. B **72**, 184434 (2005).

[39] V. I. Anisimov, J. Zaanen, and O. K. Andersen, Band theory and Mott insulators: Hubbard U instead of Stoner I, Phys. Rev. B **44**, 943 (1991).

[40] M. Yu, S. Yang, C. Wu, and N. Marom, Machine learning the Hubbard U parameter in DFT+U using Bayesian optimization, npj Comput. Mater. **6**, 180 (2020).

[41] G. Prandini, A. Marrazzo, I. E. Castelli, N. Mounet, and N. Marzari, Precision and efficiency in solid-state pseudopotential calculations, npj Comput. Mater. **4**, 72 (2018).

[42] A. Dal Corso, A. Pasquarello, A. Baldereschi, and R. Car, Generalized-gradient approximations to density-functional theory: A comparative study for atoms and solids, Phys. Rev. B **53**, 1180 (1996).

[43] V. Sahni, K.-P. Bohnen, and M. K. Harbola, Analysis of the local-density approximation of density-functional theory, Phys. Rev. A **37**, 1895 (1988).

[44] P. Giannozzi, S. Baroni, N. Bonini, M. Calandra, R. Car, C. Cavazzoni, D. Ceresoli, G. Chiarotti, M. Cococcioni, I. Dabo *et al.*, QUANTUM ESPRESSO: A modular and open-source software project for quantum simulations of materials, J. Phys.: Condens. Matter **21**, 395502 (2009).

[45] P. Giannozzi Jr, O. Andreussi, T. Brumme, O. Bunau, M. Buongiorno Nardelli, M. Calandra, R. Car, C. Cavazzoni, D. Ceresoli, M. Cococcioni *et al.*, Advanced capabilities for materials modelling with QUANTUM ESPRESSO, J. Phys.: Condens. Matter **29**, 465901 (2017).

[46] P. E. Blöchl, Projector augmented-wave method, Phys. Rev. B **50**, 17953 (1994).

[47] J. P. Perdew, K. Burke, and M. Ernzerhof, Generalized gradient approximation made simple, Phys. Rev. Lett. **77**, 3865 (1996).

[48] J. P. Perdew, J. A. Chevary, S. H. Vosko, K. A. Jackson, M. R. Pederson, D. J. Singh, and C. Fiolhais, Atoms, molecules, solids, and surfaces: Applications of the generalized gradient approximation for exchange and correlation, Phys. Rev. B **46**, 6671 (1992).

[49] H. C. Kandpal, G. H. Fecher, C. Felser, and G. Schönhense, Correlation in the transition-metal-based Heusler compounds Co_2 MnSi and Co_2 FeSi, Phys. Rev. B **73**, 094422 (2006).

[50] K. Nawa and Y. Miura, Exploring half-metallic Co-based full Heusler alloys using a DFT+U method combined with linear response approach, RSC Adv. **9**, 30462 (2019).

[51] A. Peles, GGA+U method from first principles: Application to reduction–oxidation properties in ceria-based oxides, J. Mater. Sci. **47**, 7542 (2012).

[52] R. Tesch and P. M. Kowalski, Hubbard U parameters for transition metals from first principles, Phys. Rev. B **105**, 195153 (2022).

[53] J. P. Perdew and A. Zunger, Self-interaction correction to density-functional approximations for many-electron systems, Phys. Rev. B **23**, 5048 (1981).

[54] T. Bandyopadhyay and D. Sarma, Calculation of Coulomb interaction strengths for 3*d* transition metals and actinides, Phys. Rev. B **39**, 3517 (1989).

[55] P. Collins, *The Theory of Atomic Structure and Spectra* (University of California Press, Oakland, 1982).

[56] J. R. Shewchuk, *An Introduction to the Conjugate Gradient Method without the Agonizing Pain. School of Computer Science* (Carnegie Mellon University Press, Pittsburgh, 1994).

[57] X. Gonze, Towards a potential-based conjugate gradient algorithm for order-n self-consistent total energy calculations, Phys. Rev. B **54**, 4383 (1996).

[58] F. Murnaghan, The compressibility of media under extreme pressures, Proc. Natl. Acad. Sci. USA **30**, 244 (1944).

[59] H. A. Smith, S. Elhamri, K. G. Eyink, L. Grazulis, M. J. Hill, T. C. Back, A. M. Urbas, B. M. Howe, and A. N. Reed, Epitaxial titanium nitride on sapphire: Effects of substrate temperature on

microstructure and optical properties, J. Vac. Sci. Technol. A **36**, 03E107 (2018).

[60] H. Smith, S. Elhamri, K. Eyink, Z. Biegler, R. Adams, K. Mahalingam, T. Back, A. Urbas, and A. Reed, Investigation of strain and stoichiometry of epitaxial titanium nitride on sapphire, Thin Solid Films **697**, 137832 (2020).

[61] M. Roy, N. R. Mucha, S. Fialkova, and D. Kumar, Effect of thickness on metal-to-semiconductor transition in 2-dimensional TiN thin films, AIP Adv. **11**, 045204 (2021).

[62] G. Akhtanova, Y. Yerlanuly, H. P. Parkhomenko, M. V. Solovan, A. I. Mostovyi, A. K. Nurmukhanbetova, A. V. Kireyev, I. V. Danko, P. A. Oreshkin, T. K. Zholdybayev *et al.*, Electron irradiation-induced degradation of TiN thin films on quartz and sapphire substrates, ACS Omega **9**, 925 (2024).

[63] Y. G. Khim, B. Park, J. E. Heo, Y. H. Khim, Y. R. Khim, M. Gu, T. G. Rhee, S. H. Chang, M. Han, and Y. J. Chang, Electrical conductivity enhancement of epitaxially grown TiN thin films, J. Korean Phys. Soc. **82**, 486 (2023).

[64] L. G. Parratt, Surface studies of solids by total reflection of x-rays, Phys. Rev. **95**, 359 (1954).

[65] E. Shreder, A. Makhnev, A. Lukoyanov, and K. Suresh, Optical properties and the electronic structure of Co_2TiGe and Co_2TiSn Heusler alloys, Phys. Met. Metallogr. **118**, 965 (2017).

[66] J. Barth, G. H. Fecher, B. Balke, S. Ouardi, T. Graf, C. Felser, A. Shkabko, A. Weidenkaff, P. Klaer, H. J. Elmers *et al.*, Itinerant half-metallic ferromagnets Co_2TiZ (Z = Si, Ge, Sn): *Ab initio* calculations and measurement of the electronic structure and transport properties, Phys. Rev. B **81**, 064404 (2010).

[67] B. Ernst, R. Sahoo, Y. Sun, J. Nayak, L. Muechler, A. K. Nayak, N. Kumar, J. Gayles, A. Markou, G. H. Fecher *et al.*, Anomalous Hall effect and the role of berry curvature in Co_2TiSn Heusler films, Phys. Rev. B **100**, 054445 (2019).

[68] D. B. Abraham and C. M. Newman, Equilibrium Stranskikrastanow and Volmer-Weber models, Europhys. Lett. **86**, 16002 (2009).

[69] S. V. Faleev, Y. Ferrante, J. Jeong, M. G. Samant, B. Jones, and S. S. Parkin, Unified explanation of chemical ordering, the slater-pauling rule, and half-metallicity in full Heusler compounds, Phys. Rev. B **95**, 045140 (2017).

[70] C. Ouyang, S. Shi, and M. Lei, Jahn–Teller distortion and electronic structure of $LiMn_2O_4$, J. Alloys Compd. **474**, 370 (2009).

[71] W. Kim, M. A. Smeaton, C. Jia, B. H. Goodge, B.-G. Cho, K. Lee, M. Osada, D. Jost, A. V. Ievlev, B. Moritz, L. F. Kourkoutis, T. P. Devereaux, and H. Y. Hwang, Geometric frustration of Jahn–Teller order in the infinite-layer lattice, Nature (London) **615**, 237 (2023).

[72] R. Nahar, K. M. Law, T. Roden, M. Zengel, J. Lewis, S. Budhathoki, R. Nold, H. Avlani, B. Akintunde, N. Derksen *et al.*, Dataset on density functional theory investigation of ternary Heusler alloys, Data Brief **52**, 109971 (2024).

[73] A. J. Hauser, R. E. Williams, R. A. Ricciardo, A. Genc, M. Dixit, J. M. Lucy, P. M. Woodward, H. L. Fraser, and F. Yang, Unlocking the potential of half-metallic Sr_2FeMoO_6 films through controlled stoichiometry and double-perovskite ordering, Phys. Rev. B **83**, 014407 (2011).

[74] S. Pal, S. Govinda, M. Goyal, S. Mukherjee, B. Pal, R. Saha, A. Sundaresan, S. Jana, O. Karis, J. W. Freeland *et al.*, Effect of anti-site disorder on magnetism in La_2NiMnO_6, Phys. Rev. B **97**, 165137 (2018).

[75] H. L. Feng, M. P. Ghimire, Z. Hu, S.-C. Liao, S. Agrestini, J. Chen, Y. Yuan, Y. Matsushita, Y. Tsujimoto, Y. Katsuya *et al.*, Room-temperature ferrimagnetism of anti-site-disordered Ca_2MnOsO_6, Phys. Rev. Mater. **3**, 124404 (2019).

Correction: The previously published Figure 4(b) was rendered incorrectly during the production cycle and has been set right.